Journal of Engineering and Technology for Industrial Applications

ISSN ONLINE: 2447-0228

ITEGAM-JETIA

Manaus, v.12 n.58, p.855-867. March/April, 2026.
DOI: https://doi.org/10.5935/jetia.v12i58.3116

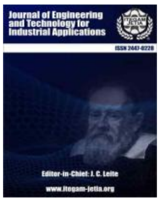

RESEARCH ARTICLE

OPEN ACCESS

SEGMENTING HEPATIC BLOOD VESSELS AND LIVER TUMORS IN CT IMAGES: AN IMPROVED EVOLUTIONARY ALGORITHM APPROACH

Selvakumar Subramanian[1], Dr. Sivakumar S[2], Dr. K. R. Ananthapadmanaban[*3]

[1, 2, 3]Department of Computer Applications, SRM Institute of Science and Technology, Kattankulathur, Chennai, India.

[1]https://orcid.org/0009-0004-6959-3251, [2]https://orcid.org/0000-0002-5073-8949, [3]https://orcid.org/0000-0001-5430-3355

Email: ss5414@srmist.edu.in, sivakums6@srmist.edu.in,*ananthapadmanabankr@srmasc.ac.in

ARTICLE INFO

Article History
Received: December 12, 2025
Reviewed: January 14, 2026
Accepted: March 10, 2026
Published: April 30, 2026

Keywords:
Liver Tumor
Barnacle Mating Optimizer
Short-term Dense Concat Segmentation Layer
Computer-aided technology
Computed Tomography.

ABSTRACT

Among the many forms of cancer, liver tumours are among the most dangerous. Liver neoplasms can be effectively predicted, identified, and managed with the help of computer-aided technology and liver interventional surgery. Accurately understanding the morphological nature of the liver and its blood arteries is a crucial task. An essential part of medical analytic planning is the segmentation of liver tumours in CT scans. The enormous difficulty, however, lies in correctly identifying and segmenting the hepatic blood veins in CT scans. Finding and segmenting hepatic vessels manually in CT scans is an inconvenient and time-consuming process. In order to segment liver tumours, this study employs a variety of techniques to clean up the input images before feeding them into the STDCSL, an algorithm for short-term dense concat segmentation. Three parts make up the STDC-CT network: detail guidance, multi-scale contextual information, and small object attention extractor. Small affected area attention guides the merging of detailed and contextual information branches. This study proposes an improvement to the Barnacle Mating Optimizer (BMO), an evolutionary algorithm that takes its cues from nature, in order to fine-tune the STD-CSL parameters. Levy flight is used to enforce and replace the sperm cast equation, which improves the exploration phase of the original BMO. Next, the enhanced BMO (IBMO) is teamed up with the suggested STDCSL. The technology proves to be reliable and applicable to automatic analysis of liver tumours in everyday clinical practice, proving its generalizability. The method's great accuracy in stroke detection further supports its potential use as a clinical tool for preoperative clinical planning.

I. INTRODUCTION

Liver tumours pose a threat to people's lives and well-being globally; they are the second most deadly malignancy in terms of morbidity and death [1]. Liver tumour segmentation is the initial phase in the computer-aided diagnostic method for liver cancer, which is currently often employed in the diagnosis and treatment planning process using human abdominal computed tomography (CT) [2]. This process involves separating tumours from nearby organs and tissues in CT scans. While other imaging tests, including as ultrasonography and MRI, can aid in the diagnosis of cirrhosis, computed tomography (CT) is the gold standard [3]. A CT scan is a thorough kind of imaging because it produces detailed cross-sections of the abdomen.

Problems with tumour and lesion homogeneity during CT scan segmentation have been reported [4]. Liver tumour segmentation is not a good fit for the outcome. Accordingly, improved photos are suggested for better accuracy. The CT scan finds the tumour by noticing a change in the intensity of the pixels in the liver [5]. Hypodense tissue refers to the area of the liver that appears darker in comparison to the surrounding tissues. Furthermore, it has been noted that traditional tumour segmentation methods are computationally intensive [6]. Given the circumstances, a clinical setting would be less than optimal. A CT scan of the liver will typically show more than 150 slices, which is considered normal. Both the tumour and its surrounding areas exhibit low contrast and a great deal of form irregularity [7].

Computer Aided Design (CAD) technologies are currently the focus of global research efforts aimed at segmenting liver tumours from abdominal CT scans [8]. The current state of tumour segmentation is unreliable and ineffective due to its reliance on edge detectors. One of the techniques created for autonomous tumour segmentation using Deep Learning (DL) is the CNN [9]. CNNs remain a popular method among researchers for segmenting liver tumours. The diverse forms of liver tumours, along with low contrast and indistinct borders with nearby organs besides tissues, make tumour segmentation from liver CT images an arduous task, despite the attention of many scholars to this problem [10].

It is difficult to segment the liver tumour due to the surrounding muscle and the blurring borders caused by the slight difference in grey scale contrast between the tumour and other organs (e.g., the heart, kidneys, etc.) [11]. The liver tumour segmentation job is further complicated by the fact that tumour size and position might fluctuate from person to person, and that tumours can span numerous CT slices with small variations between them [12]. Consequently, recent studies have shown that a combination of deep learning and techniques based on local information works well. Many intensity-based methods have been created for the purpose of segmenting tumours and livers from CT images by statistically analysing their intensities [13]. Level set based active contour techniques are one of these more independently deployable alternatives.

In better match the liver tumor border in the test CT image, a level set contour - based technique is used to produce a coarse segmentation initial mask [14].The aforementioned models have shown promise in certain contexts, however input images with high resolution, complicated settings, and many small affected areas may not be suitable for their performance [15], [16]. It is also difficult to accomplish real-time, high-quality semantic segmentation due to the limited computing resources. Consequently, accomplishing real-time in semantic segmentation tasks while enhancing segmentation quality. The chief goal of this research is to mature a method for better liver tumour segmentation using input photographs.

- The purpose of this research is to contemporaneous a framework for tumour segmentation using target CT scans.
- The segmentation accuracy is enhanced by adjusting the parameters of the suggested model, which is integrated with the original Barnacle Mating Optimizer (BMO), which was enhanced by Levy Flight, in order to detect and divide up liver tumours.
- The Tversky loss function is employed to address the issue of severely imbalanced foreground and background voxels.
- Various metrics are used to conduct investigates on the publicly available LiTS dataset and the 3D-IRCADb01 dataset.

The break of the paper is prearranged as shadows: Section 2 mentions the related works; Section 3 provides the proposed organization with its mathematical expression; Section 4 mentions the result analysis and Section 5 concludes the research contribution.

II. RELATED WORKS

Using a single framework that combines segmentation and uncertainty estimation [17] provide a new reliable multi-phase liver tumour segmentation method called TMPLITS. Clinicians could benefit from the trustworthy outcomes in making a dependable diagnosis. For the purpose of parameterizing the segmentation besides uncertainty using evidence following the Dirichlet distribution, Dempster-Shafer Evidence Theory (DST) is specifically introduced. It is specifically defined how reliable the segmentation results are over multi-phase CECT images. However, to ensure the efficacy of the fusion technique grounded in theoretical analysis, a multi-expert is suggested for merging the multi-phase evidences. When tested against state-of-the-art approaches, TMPLiTS proved to be the clear winner. At the same time, we have confirmed that TMPLiTS is resilient, so we know that it will reliably work even when faced with disturbances. For better picture segmentation and to make better use of image spatial data [18] suggests an improved network construction called ELTS-Net that is based on the 3D U-Net model.

This would solve the problems caused by traditional approaches and the 2D U-Net network configuration. ELTS-Net improves upon the first network by enhancing the convolutional kernel's receptive field with dilated convolutions. In addition, the original convolutional module is replaced by an attention residual module, which primarily functions as an encoder and decoder. This module includes an attention mechanism and residual connections. The network may now gather channel and spatial contextual information on a global scale thanks to this design. In addition, the decoder network has deep supervision modules at several levels to supplement intermediate-level feedback. In doing so, we optimise the segmentation findings by limiting the network weights to the target regions. Results on the LiTS2017 dataset demonstrate that, in comparison to the model, the model performs better on liver and tumour segmentation tasks. The model achieves an accuracy of 95.2% for liver segmentation and 71.9% for tumour segmentation, representing an improvement of 0.9% and 3.1%, correspondingly.

The experimental consequences provide useful assistance for clinical diagnosis and therapy by validating ELTS-Net's superior segmentation performance compared to other comparator models.To overcome these obstacles [19] suggested SBCNet, a new model for dual-branch liver tumour segmentation. Better identification of tumour variability utilising an enhanced multi-scale adaptive kernel is made possible by our suggested method's contextual encoding module. In addition, the corresponding branch has a boundary enhancement module that uses contour learning in conjunction with the Sobel operator to improve boundary perception. Lastly, in order to further improve tumour segmentation, we suggest a hybrid multi-task loss function that takes into account both the size and boundary features of tumours at the same time. This will encourage interaction between the various tasks of the dual branches. With SBCNet producing competitive results when compared to other state-of-the-art algorithms for liver tumour segmentation, experimental validation using the publically accessible LiTS dataset proves the practical module.

First of its kind [20] suggests a dual-stream multi-level fusion outline (DM-FF) for direct accurate segmentation of liver tumours from non-contrast multi-modality images. In order to efficiently extract multi-level feature maps that correspond to a predefined representation of each modality, our DM-FF first builds an attention-based encoder-decoder. Then, DM-FF builds two kinds of fusion modules: one that uses learned features to get a common representation images, which lets you take advantage of similarities and boost performance, and another that uses segment decision evidence to find differences between modalities, which helps you avoid interference caused by conflicts between modalities. With the help of these three parts, DM-FF can accurately segment multi-modality non-contrast images by letting them work together.

When compared to eight state-of-the-art segmentation architectures, DM-FF improves performance and achieves a Dice of 81.20% in an evaluation on 250 patients using two MRI scanners and a variety of tumour types. According to the findings, our DM-FF greatly encourages the creation and use of non-contrast liver tumour imaging techniques. The attention connect network (AC-Net) was developed for automatic liver tumour segmentation and introduced by [21]. Our method, which is based on the U-shaped network construction, uses two crucial attention module (AAM) besides the vision transformer module (VTM)—to integrate spatial elements seamlessly, replacing conventional skip-connections. The VTM processes low-resolution feature maps using multihead self-attention and then reshapes the output into a feature map for later concatenation; the AAM computes axial attention across feature maps to enable feature fusion. In addition, we use a loss function that is exclusive to our method. We commence our procedure by pretraining AC-Net on the LiTS2017 dataset, and then we refine it with CT and MRI data obtained from Hubei Cancer Hospital.

Measurements for AC-Net's performance on CT data are as follows: a recall of 0.92, a Jaccard coefficient (JC) of 0.82, an normal symmetric surface distance (ASSD) of 4.59, a accuracy of 0.89. Metrics for AC-Net on MRI data are as follows: DSC = 0.80, JC = 0.70, recall = 0.82, ASSD = 7.58, HD = 30.26, pinpoint = 0.84. For the purpose of liver image segmentation [22] propose using hyper tangent Fuzzy C-Means (HTFCM). It got segmentation results that were nearly identical to the ground truth liver images by calculating the data point distance from the cluster centres using hyper tangent distance. Unfortunately, the liver images are too fuzzy for any state-of-the-art model to accurately pinpoint the tumours. However, the proposed model manages to do just that. This research shortened the processing time for early liver disease diagnosis, increased classification accuracy, and resolved the linear mapping problem using fuzzy logic. While classifying liver tumours, the suggested model improves accuracy to 99.58% and time by 2-25 s.In their ground-breaking AI-driven framework for liver tumour prediction [23] have brought together state-of-the-art methods to increase analytical depth and accuracy.

Histological Genomic Feature Extraction (MIRSLiC) are both included into the framework, which allows for a detailed comprehension of molecular markers and precise tumour segmentation in medical imaging. Furthermore, a multidimensional feature extraction module integrates acoustics, clinical data, videomics, and radiomics to produce a complete dataset. All of these factors work together to form a cohesive model that can predict tumour features, subtypes, and prognosis with great precision. Reliability is emphasised through model review and continual improvement integrative technique breaks new ground in liver tumour prediction by giving doctors practical information for individualised treatment plans. The model is tested extensively on various datasets, and the results show that it is accurate and reliable. Our model demonstrates remarkable accuracy and resilience in tumour segmentation, with a recall rate of over 92%, a precision of over 87%, and a Dice coefficient of over 0.89. Survival prediction accuracy in prognostic modelling routinely exceeds 84%, demonstrating the model's capacity to offer useful insights into the future course of liver cancer.

III. PROPOSED METHODOLOGY

In this section, the brief elucidation of liver cancer segmentation is mentioned with its mathematical expression from CT scan images. Figure 1 mentions the workflow of the proposed model.

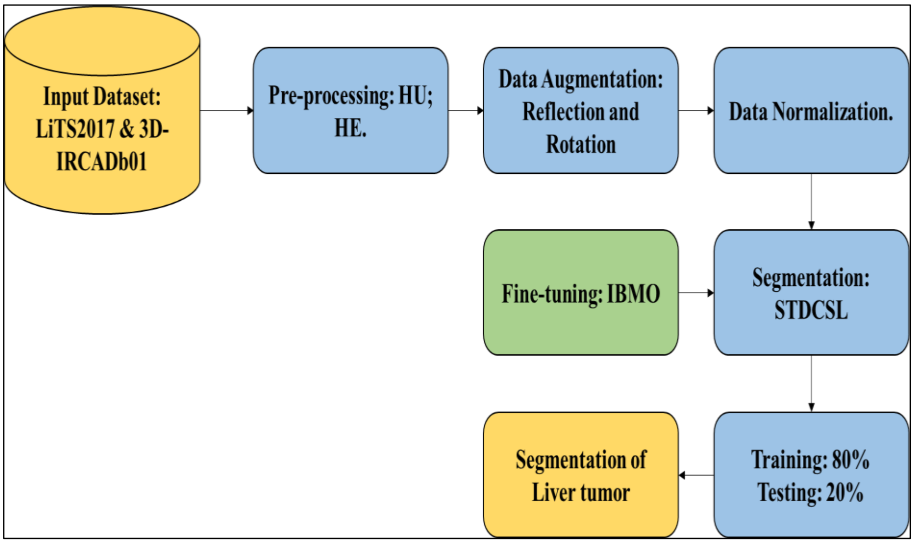

Figure 1: Workflow of the Research Work.
Source: Authors, (2026).

III.1 DATASETS

Popular datasets include 3DIRCADb, which is used to compare 3D picture reconstruction methods, and the LiTS2017 dataset, which is the official dataset given by the joint organising of MICCAI and ISBI competition for liver and liver tumour segmentation. Improvements in medical picture segmentation methods and a more fair evaluation of new approaches to liver tumour segmentation are the intended outcomes of these endeavours. Included in the LiTS2017 dataset are 201 CT images of humans. The official has annotated 131 of the 201 CT images, while the remaining 70 are raw CT scans without any commentary. The 70 in question served as the competition's performance test dataset, which explains why. Tumour diameters varied from 38 to 349 cubic millimetres, while the number of tumours per patient varied from 0 to 75. The data varied somewhat in quality because it came from a wide variety of universities using different technology. These slice samples had a resolution between 0.55 and 1.0 mm, a range of 0.45 to 6.0 mm for the spacing between slices, and 42 to 1026 slices for the total number of slices. Figure 2 presents the sample image of LiTS2017.

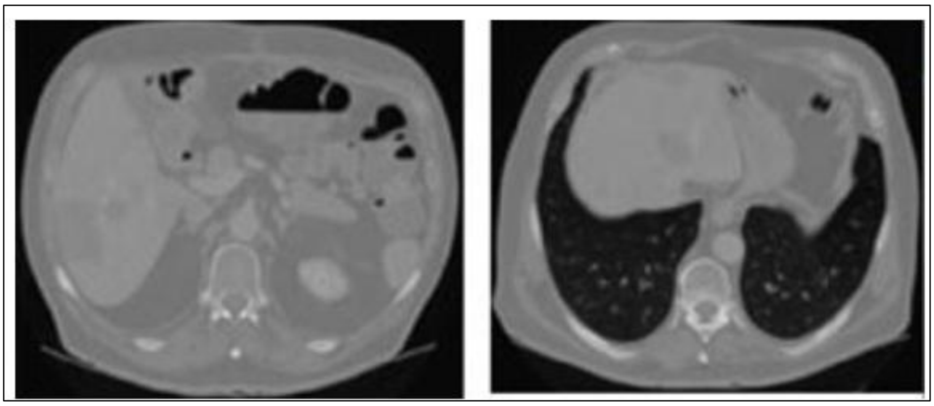

Figure 2: Sample of LiTS2017 dataset.
Source: Authors, (2026).

Three datasets, 3DIRCADb-02 and 3DIRCADb-01 [24], make up the 3DIRCADb dataset. While there are no liver tumours in the 3DIRCADb-02 dataset, there are 75 percent of cases with liver tumours in the 3DIRCADb-01 dataset, with tumour numbers ranging from 1 to 46. With dimensions ranging from 16.3 to 24.9 cm, 12.0 to 18.6 cm, and 11.0 to 20.2 cm, respectively, and voxel sizes ranging from 0.56 to 0.87 cubic millimetres, 1.6 to 4.0 cubic millimetres, the image had a resolution of 512 × 512 pixels. Figure 3 presents the sample image of 3DIRADb dataset.

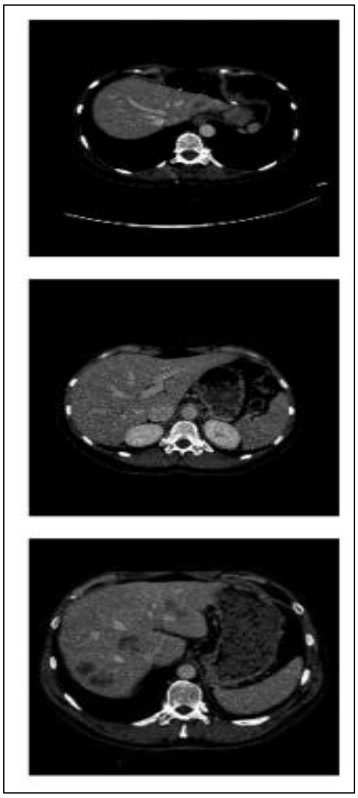

Figure 3: Sample image of 3DIRADb dataset.
Source: Authors, (2026).

III.2 IMAGE PRE-PROCESSING

Each slice was pre-processed as detailed in the following sections so that the liver could be differentiated from nearby organs.

III.2.1 Hounsfield Windowing (HU)

The Hounsfield unit (HU) is used in computed tomography (CT) scans to evaluate tissue density. The HU is specified as −1000 for air, zero for water, and +1000 for bone. Table 1 shows that the HU values for many organs and fluids fall somewhere in the middle of this range. In a typical windowing operation, the CT component of the image, allowing the operator to focus on certain tissues of interest. You can change the image's brightness using the window level. Shifts the focus by adjusting the width of the window.

$$HU = 1000 \times \frac{\mu tissue - \mu H_2O}{\mu H_2O} \tag{1}$$

By assigning a grayscale intensity to each value, the HU value is determined for each pixel; pixels with higher values are considered brighter. Navigate the DICOM slides using Hounsfield Windowing and adjust the range to [−100, 400] [−100, 400] [25].

Table 1: Hounsfield unit standards define for body organ.

Value for Body Organ	**HU**
1000	Bone
40 to 60	Liver
46	White Matter
43	Grey Matter
40	Blood
10 to 40	Muscle
30	Kidney
15	Cerebrospinal
0	Water
−50 to −100	Fat
−1000	Air

Source: Authors, (2026).

The liver can be better seen by applying HU windowing at each slice, with a HU range of −100 to 400 chosen. Although the image and organs got, it is evident that most organs are obstructed in CT image slices without the procedure. Hence, all slices undergo this HU windowing before being passed on to the subsequent phase.

III.2.2 Histogram Equalization

The liver and its surrounding tissues were not easily distinguishable, even though HU windowing allows for excellent organ visualisation. The resultant picture was normalised within the range of [0, 1] after applying histogram equalisation following window processing.

III.3 DATA AUGMENTATION

Every scan in the datasets under consideration has its unique tumour mask that denotes the tumor's and liver's precise position. Nevertheless, deep learning training cannot be conducted with the number of tumor-containing slices. So, the combined slice and its mask were subjected to data augmentation techniques like reflection, flipping, and rotation. To put it simply, data augmentation will boost network accuracy by increasing picture spatial variation [26]. The two methods of data enhancement that were employed are these:

III.3.1 Reflection

One way to increase the amount of data used to train a network is through reflection, which involves flipping the image along the x or y axis. The computational expense can be reduced by reflecting the liver pictures with their tumour masks.

III.3.2 Rotation

As a data augmentation technique, rotation entails turning the image to a new degree, effectively creating a new image. The photos of the liver and its masks are rotated by 90 degrees here.

III.4 IMAGE NORMALIZATION

A method for lowering inter-patient of picture intensities in a dataset is image intensity normalisation [27]. It will also lead to better segmentation results and make patient images more comparable. Hence, intensity normalisation is applied to liver CT scan results.

III.5 SEGMENTATION USING SHORT-TERM DENSE CONCAT SEGMENTATION LAYER (STDCSL)

Based on the STDC module's layout illustrated by the BiSeNet [28] model, the study effort suggests a new STDC backbone network. With the goal of improving real-time semantic segmentation performance, a new Detail Guidance Unit has been developed to supersede the original Spatial Path branch of BiSeNet. This module keeps low-level detail features while lowering the computational cost of the network. Nevertheless, there are still certain limitations to this network when it comes to segmenting small affected areas. For tiny impacted area segmentation tasks in particular, the detail information that the FFM module loses when it gradually reduces the maps could be beneficial. Additionally, the accuracy of tiny impacted area segmentation may be compromised due to the Detail Guidance Module in the STDC-Seg network primarily concentrating on low-level feature layers, potentially ignoring certain detail information in higher-level feature layers. So, here we present the STDC-CSL network, a new approach to small-scale segmentation that promises to be both accurate and fast.

III.5.1 Small Object Attention Extractor for STDC

So that the STDC backbone network could extract more useful features for minor recognition, we built (SOAE) module. From Stage 3 through Stage 5, we used convolutional layers with varying resolutions to extract various features from the input data. Different convolutional layers capture features at different scales by operating at varying resolutions. Then, to get a fuller picture, we combined the most useful features using an attention mechanism that picked them out automatically.

In particular, we set maps $F_i(i = 1,2,3)$ produced by Stages 3 to 5 as $T^t(t = 1,2,3)$, as seen in Figure 4. Afterwards, a 1 × 1 convolutional layer with a size decreased to 1 was used to pass the template layer T^t. Afterwards, a fully connected to construct the maximum map, which entails capturing the most significant feature pixels and mapping them to vectors for computation.

$$S_t^i = Similarity(T^t, T^i) = \frac{T^t \times T^i}{\|T^t\| \times \|T^i\|} = \frac{\sum_{j=1}^{n} T^t j \times T^i j}{\sqrt{\sum_{j=1}^{n} T^t j} \times \sqrt{\sum_{j=1}^{n} T^i j}} \tag{2}$$

Where S_t^i represents the cosine similarity among the template layer T^i and T^t. $T^t j$ and $T^i j$ signify the corresponding to T^t and T^i, respectively. For instance, when T^1 serves as the template, values S_1^2 between T^2 and T^1, and S_1^3 between T^3 and T^1, indicate the attention levels of T^2 and T^3 toward T^1, respectively, while $S_1^1 = 1$. Likewise, when T^2 serves as the pattern, the cosine resemblance values S_1^2 between T^1 and T^2, and S_2^3 between T^3 and T^2, designate levels of T^1 and T^3 toward T^2, respectively, while $S_2^2 = 1$. To evaluate the attention weights a_t^i, we input $\{S_t^1, S_t^2, S_t^3\}$ into weight values:

$$a_t^i = \frac{exp(s_t^i)}{\sum_{i=1}^{3} exp(s_t^i)} \tag{3}$$

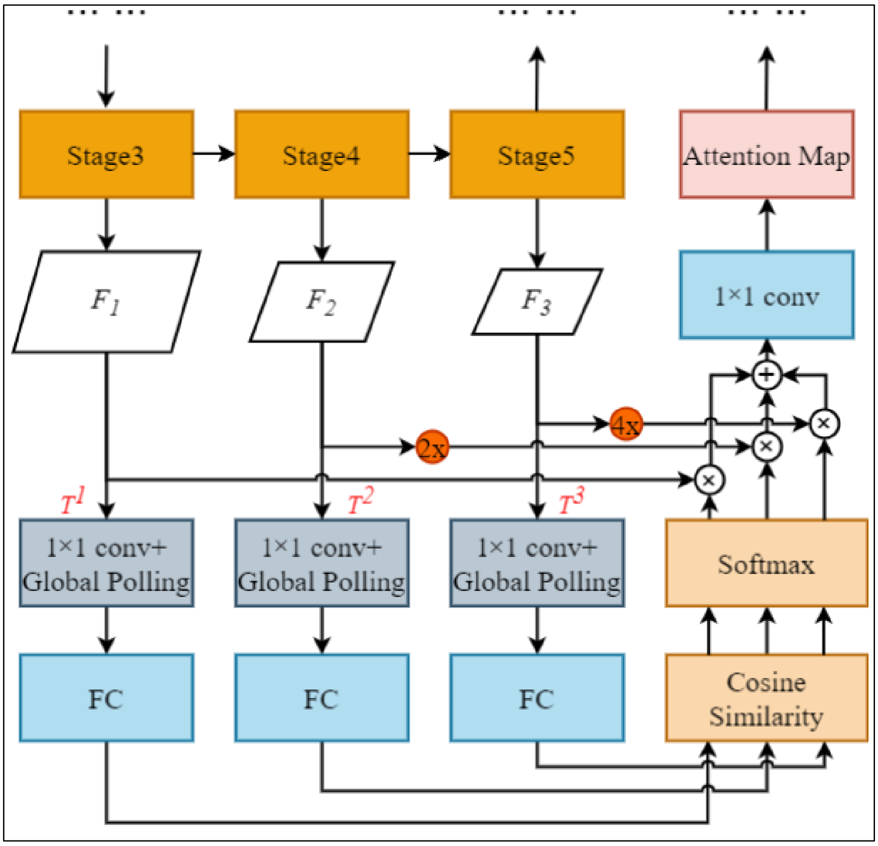

Figure 4: The small area attention extractor module.
Source: Authors, (2026).

The feature map sizes F_1 must remain constant after acquiring the attention weights, matching that of F_1; thus, we unsampled F_2 and F_3 by 2× and 4×, correspondingly, and the number of channels of F_1, F_2, and F_3 were 256, 512 and 1024 respectively. To acquire the attention feature, we first added the weighted levels one by one, and then attuned the sum of channels using a 1 × 1 convolution.

$$A_t = \sum_{i=1}^{3} a_t^i \times F_i \tag{4}$$

Where A_t signifies the attention feature gotten finished the network with T^t as the template layer.

III.5.2 Laplacian of Gaussian for Detail Guidance Unit

The STD-CSL network used the Laplacian convolution approach to extract precise features of picture edges. Due to its high quality, the Laplacian operator has seen extensive application in edge detection applications. In order to identify noticeable changes in pixel intensity, edge detection frequently employs the Laplacian operator. Consequently, the Laplacian operator might incorrectly boost the edges of tiny objects as noise. The Laplacian operator is very sensitive to noise, which is not surprising given that it can appear anywhere in a picture. Pixels around small objects can be subject to a high reaction from noise when the operator is applied, resulting in the noise signal overshadowing the margins of the objects. Thus, edge detection could incorrectly eliminate tiny objects' edges since they are thought of as noise.

We use the Laplacian convolution approach in the Detail Guidance Module to fix these shortcomings while keeping the Laplacian operator's superior edge extraction capability. The LoG convolution method differs from the Laplacian convolution method in that it employs Gaussian filtering to minimise noise and blur high-frequency features before convolution. Reducing the impact of noise is achieved by creating space between the edges of tiny objects and the noise. In addition, the gradient variations near the margins of the image are diminished by using Gaussian filtering. Edge gradient fluctuations are quite sensitive to the Laplacian operator, and noise, which usually contains a high-frequency component, is also very sensitive to this operator.

As a result, small object edges can be more easily detected with the use of Gaussian filtering, which reduces noise interference by lowering changes in edge gradients. By applying a Gaussian filter and Laplacian convolution on the images, we can reduce the influence of noise while maintaining the Detail Guidance Module's exceptional edge extraction performance. The precision of edge detail extraction can be enhanced using this approach. Utilising the operation—which involves merging the Gaussian function and the Laplacian operator into a single kernel—allows us to decrease computing overhead. This means the picture just needs one convolution process. Here is the procedure for merging methods:

There is the Gaussian equation:

$$gauss(x, y, \sigma) = \frac{1}{2\pi\sigma^2} exp\left(-\frac{x^2+y^2}{2\sigma^2}\right) \tag{5}$$

The two-dimensional Gaussian function is transformed using the Laplacian operator.:

$$\begin{aligned}\nabla^2\big(gauss(x, y, \sigma)\big) &= \frac{\nabla^2(gauss(x,y,\sigma))}{\partial^2 x} + \frac{\nabla^2(gauss(x,y,\sigma))}{\partial^2 y} \\ &= \frac{1}{2\pi\sigma^2}\frac{\partial\left(-\frac{x}{\sigma^2}exp\left(-\frac{x^2+y^2}{2\partial^2}\right)\right)}{\partial x} + \frac{1}{2\pi\sigma^2}\frac{\partial\left(-\frac{y}{\sigma^2}exp\left(-\frac{x^2+y^2}{2\partial^2}\right)\right)}{\partial x} \\ &= \frac{1}{2\pi\sigma^4}\left(\frac{x^2}{\sigma^2} - 1\right) exp\left(-\frac{x^2+y^2}{2\sigma^2}\right) + \frac{1}{2\pi\sigma^4}\left(\frac{y^2}{\sigma^2} - 1\right) exp\left(-\frac{x^2+y^2}{2\sigma^2}\right) \\ &= \frac{1}{2\pi\sigma^4}\left(\frac{x^2+y^2}{\sigma^2} - 2\right) exp\left(-\frac{x^2+y^2}{2\sigma^2}\right)\end{aligned} \tag{6}$$

where x and y designate the copy pixel organizes, $\nabla^2(gauss(x, y, \sigma))$ signifies the LoG operator.

III.5.3 PAPPM for Capturing Contextual Information

Researches suggested a method called parallel aggregation pyramid pooling unit (PAPPM) [29] to improve the neural network's efficiency in capturing multi-scale contextual information. In order to extract pooling maps at various scales, the PAPPM module is divided into four parallel branches. Each branch uses a different pooling kernel size. Concatenating these traits allows for the effective acquisition of contextual information at several scales. The module minimises processing cost without sacrificing accuracy by utilising parallel computation to speed up the inference process. In Figure 5, we can see the PAPPM module connected to the STDC network.

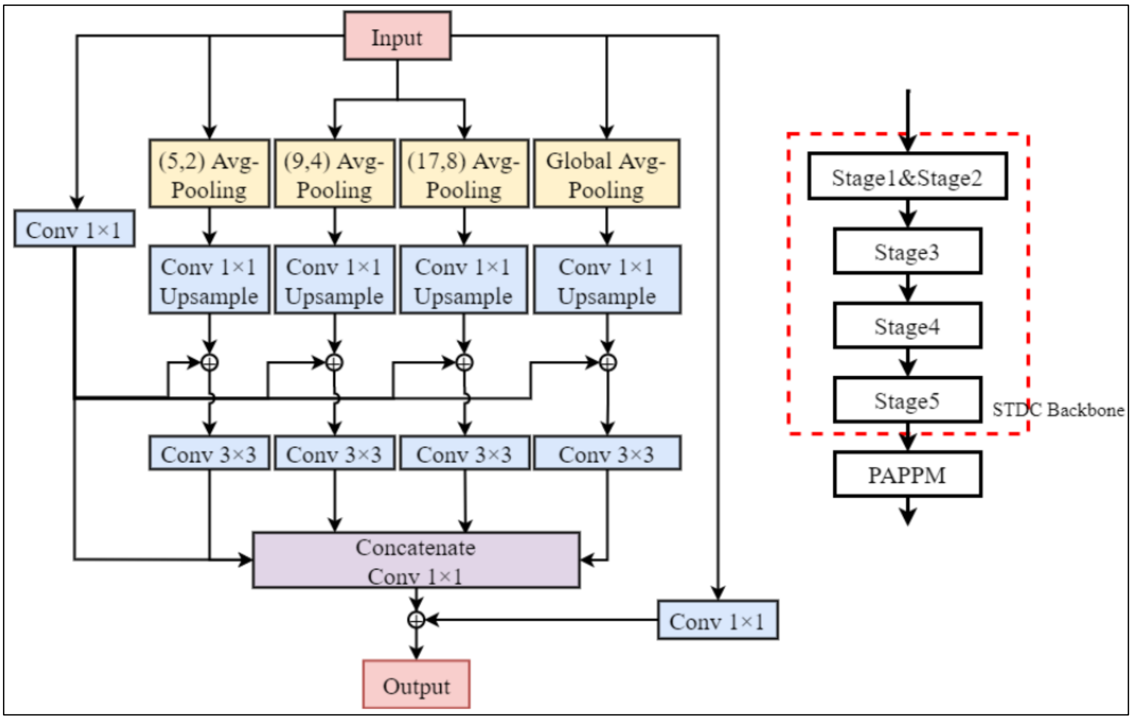

Figure 5: The PAPPM network architecture.
Source: Authors, (2026).

III.5.4 The Part and Context Feature Fusion Unit

The context branch of the STDCSL network is a treasure trove of semantic information that can improve the network's semantic representations. The continual downsampling process, however, causes it to lose a great deal of geometric and spatial information. While designing the SOAE module, we used its small object attention characteristics to guide the detail info, ensuring that the STDCSL network had a good mix of detail and contextual data. Reason being, STDCSL network accuracy in small object segmentation from input images was one of the primary goals while it was being designed. Hence, we align the merger of detail and contextual information with the small object attention branch, which we trust greatly, besides use it as variable. In the suggested method, the attention feature is initially normalised by passing it through a sigmoid layer, which yields the weight value w. Here, w represents the detail features' weight parameter and 1 − w stands for the contextual information's weight parameter. After that, feature fusion is done by multiplying the detail features and contextual info by their respective weight values, and then adding the results. The last step in obtaining Fout is to run the features through a CONV-BN-ReLU. Figure 6 shows the method's detailed structure.

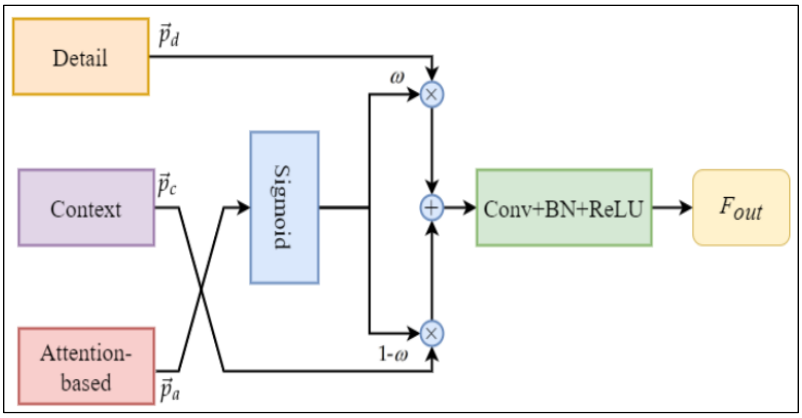

Figure 6: Detail and context feature fusion module.
Source: Authors, (2026).

The a, c, and d branches stand for the little attention, context, and detail aggregation module branches, respectively. You may see the outcomes of these branches as pixel vectors labelled with the symbols $\vec{p}_a$, $\vec{p}_c$ and $\vec{p}_d$, correspondingly. The demonstrations of w and Fout can be written as shadows:

$$\omega = Sigmoid(\vec{p}_a) \tag{7}$$

$$F_{out} = ConvX\big((1-\omega)\otimes\vec{p}_c + \omega\otimes\vec{p}_d\big) \tag{8}$$

Where the layers for convolution, batch normalisation, and ReLU activation make up ConvX. The model's training gives more weight to the detail characteristics when w > 0.5, and more weight to the contextual information when w < 0.5.

III.5.5 Softmax and Loss Calculation

After every layer except the bottom one's feature maps have been decreased in dimension, a Softmax layer processes them. After that, labels with a corresponding resolution are obtained by trilinear interpolation downsampling, and the loss for each map is computed against them. Multiple network paths can now independently calculate losses and update weights thanks to this design. This is the total loss function, as understood in Equation (9).

$$L_{total} = L_{all} + \sum_{d=1}^{3} L_d \tag{9}$$

In the formula: L_{all} is the loss fusion; L_d is for the dth layer. Due to the fact that hepatic vascular segmentation becomes a multi-task learning process under multi-resolution deep supervision, and each path's parameter update is equally significant, the loss weights of the many supervised equal. Output Prediction: Finally, the last feature map is sent into the Softmax layer to get the segmentation prediction. By considering the hierarchical structure of the feature maps and the varied resolutions, this multi-resolution depth supervision method computes the total loss function in a more sophisticated and efficient manner. The parameters of many supervised pathways are initially set at random since each path has its own target. So that the network doesn't get stuck in a rut, each training path improves the network's semantic expression, and the parameters are changed separately without affecting each other. This network has the ability to segment tiny hepatic vessels because it can context info for fusing feature maps of prediction outcomes. To illustrate the disparity between the classes, this research makes use of the Tversky loss function. Equation (10) shows how it is defined by Tversky.

$$L_T(P,G,a,\beta) = \frac{|P \cap G|}{|P \cap G| + a|P-G| + \beta|G-P|} \tag{10}$$

In the formula: P is the forecast label; G is the footnote label; |P ∩G| is the entire sum of that are truthfully secret; |P − G| characterizes the sum of false positives that are voxels; |G − P| is the entire that voxels; |P − G| + |G − P| signifies the sum of all voxels that were incorrectly categorised. A part of it involves controlling the trade-off among changing α and β. Equation (11) defines the Tversky loss function:

$$T(a,\beta) = \frac{\sum_{i=1}^{N} p0_i g0_i}{\sum_{i=1}^{N} p0_i g0_i + a\sum_{i=1}^{N} p0_i g1_i + \beta\sum_{i=1}^{N} p1_i g1_i} \tag{11}$$

In the formula: in the Softmax layer's output, 〖p0〗 _i denotes the voxel i is a foreground voxel, 〖p1〗 _i denotes the likelihood that voxel i is a background (non-liver blood vessel) voxel, and 〖g0〗 _i and 〖g1〗 _i represent, respectively, the fore- ground in the label. A prime number whose value is either 1 or 0, denoted by its label. One may find the loss gradient in relation to p0i and p1i in the given equation using Equations (12) and (13), respectively:

$$\frac{dT}{dp0_i} = 2\frac{g0_j(\sum_{i=1}^{N} p0_i g0_i + a\sum_{i=1}^{N} p0_i g1_i + \beta\sum_{i=1}^{N} p1_i g0_i)}{\left(\sum_{i=1}^{N} p0_i g0_i + a\sum_{i=1}^{N} p0_i g1_i + \beta\sum_{i=1}^{N} p1_i g0_i\right)^2} - \frac{(g0_j + a g_{1j})\sum_{i=1}^{N} p0_i g0_i}{\left(\sum_{i=1}^{N} p0_i g0_i + a\sum_{i=1}^{N} p0_i g1_i + \beta\sum_{i=1}^{N} p1_i g0_i\right)^2} \tag{12}$$

$$\frac{dT}{dp1_i} = \frac{-\beta g1_j\sum_{i=1}^{N} p0_i g0_i}{\left(\sum_{i=1}^{N} p0_i g0_i + a\sum_{i=1}^{N} p0_i g1_i + \beta\sum_{i=1}^{N} p1_i g0_i\right)^2} \tag{13}$$

Training weight balancing is unnecessary for the Tversky loss function. It is possible to regulate the trade-off adjusting the hyperparameters α and }. Experiments confirm that the effect is optimal and accuracy is optimum when α = 0.3 and β = 0.7.

III.5.6 The Process of Post-Processing

To recover the presentation of the network model, the hepatic vessels predicted by the model are further processed in the post-processing stage. At this stage, it is necessary to determine every linked domain. We established an empirical criterion to differentiate between noise and real hepatic vessels: linked zones smaller than 180 mm3 are regarded as noise. In light of the fact that a lower threshold could retain too much noise and a higher one could eliminate huge detached vessels, this is a well-balanced option based on our experience. In this context, "disconnected blood vessels" mean breaks in vascular continuity seen in imaging. These breaks could be caused by physical or pathological alterations to the vessels, algorithmic flaws in image processing or segmentation, or just plain old limitations in the quality of the imaging itself. Misclassification in segmentation can be mitigated by including a post-processing phase that decreases improper noise removal.

III.5.7 Fine-Tuning Of The Model Using Improved Barnacle Mating Optimizer

A bio-inspired procedure called the Barnacles Mating Optimizer (BMO) was projected in [30] and is based on the mating behaviour of barnacles. During mating, barnacles use a sperm-casting strategy in addition to the standard copulation method. Normal copulation in BMO is viewed as an exploitative activity based on the Hardy-Weinberg principle's idea, in contrast to the exploratory approach exemplified by the sperm cast. The next section will discuss how the exploration phase is where the original BMO gets improved.

A) Initialization

The barnacle population, which can be expressed as follows, is the contender for initialization in solution X:

$$X = \begin{bmatrix} x_1^1 & \cdots & x_1^N \\ \vdots & \ddots & \vdots \\ x_n^1 & \cdots & x_n^N \end{bmatrix} \tag{14}$$

Each population is assessed, and the optimal solution is ranked according to its performance, where n is the overall populace size and N is the sum of control variables to be optimised.

B) The procedure of selection for parents to be mated

The length of penis, or pl, is a pre-determined measure that is used to pick two parents of barnacles. All of the assumptions made in [30] will be used in this paper.

C). Barnacles' off-spring reproduction procedure

Here are several idioms that describe the process of BMO reproduction:

$$x_i^{N\_new} = p x_{barnacle\_d}^N + q x_{barnacle\_m}^N \tag{15}$$

$$x_i^{N\_new} = rand() \times x_{barnacle\_m}^N \tag{16}$$

$x_{barnacle\_d}^N$ and $x_{barnacle\_m}^N$ where q = 1 - p is the random variable representing the parents of barnacles, and where p is a normally distributed integer. The basic random integer [0-1] is used in this algorithm as rand().

D). Implementation of Levy flights

When it comes to determining BMO's exploration and exploitation procedures, the pl value is paramount. The use of basic random numbers to produce new generations is viewed as an exploratory procedure, as can be seen from Equation (17). The following expression is substituted for Equation (17) to enhance the exploration process in this work.:

$$x_i^{N\_new} = x_{barnacle\_m}^N + Levy(N) \tag{17}$$

Where Levy flight is strong-minded as shadows:

$$Levy(N) = 0.01 \times \frac{r_1 \times \sigma}{|r_2|^{\frac{1}{\beta}}} \tag{18}$$

β is a continuous set to 1.5, r_1 and r_2 are accidental statistics [0-1], besides the equation is as shadows:

$$\sigma = \left(\frac{\tau(1+\beta) \times \sin\left(\frac{\pi\beta}{2}\right)}{\tau\left(\frac{1+\beta}{2}\right) \times \beta \times 2^{\left(\frac{\beta-1}{2}\right)}} \right)^{\frac{1}{\beta}} \tag{19}$$

where $\tau(y) = (y-1)!$

The first step in the IBMO process flow is to establish an X population and begin producing new offspring. The next step is to assess the new generation before combining them with the parents. Prioritising the best answer at the moment is achieved by sorting the population. The following iteration is supposed to delete the lowest half of the populace and evaluate only half of the top populace, which is a mixture of parents and children.

Finding the optimal set of variables that yields the lowest objective evaluation is the goal of the IBMO Algorithm. Keeping to all restrictions while minimising forecast mistakes is the goal of this work. A number of initial parameters are defined, including pl, total populace, and maximum details, like the test system data and the seeking area boundaries, are determined. The data of the chosen test system is then temporarily saved with each population's control variables. There can be no more than fifty iterations. The results indicated in Table 2 can also be achieved with this population size.

Table 2: Property setting of proposed algorithm.

Values	Property
50	Populace size
50	Maximum Iteration
1	Lower-bound
1000	Upper-bound

Source: Authors, (2026).

IV. RESULTS AND DISCUSSION

Our development environment for training and testing the proposed model includes python 3.9.1, an i7 processor running at 2.25 GHz with 16 cores, and Ubuntu versions 20.04 LTC and 18.04 LTS. Adam optimizer updates the network weight during training using a learning rate of 0.0001 besides a minibatch size of 16. The ResU-Net is trained using the TensorFlow and Keras deep learning libraries on top of the $NVIDIA\ Tesla\ T4\ GPU$ Colab, which is powered by Google. Over both simulated and real-world photos, the suggested strategy was evaluated and found to be effective.

IV.1 EVALUATION METRICS

Our research involves a careful extraction of blood vessel labels from this dataset in order to conduct an extensive experimental investigation. By utilising these datasets, we can guarantee that our research is in line with present norms and does in medical picture segmentation, and we also provide a strong foundation for our experimental processes. In this study, we used a cross-validation strategy to assess the method's presentation. Each round of validation utilised one subset of the datasets as the test set and the residual subsets as the training set. The datasets were separated into k subsets in total.

The procedure was carried out k times, with set precisely once. In this article, we employ voxel segmentation overall segmentation accuracy assessment's coincidence rate (Dice) as evaluation markers. The Dice measure of the overlap of two pictures; its value ranges from 0 to 1, and it indicates the rate of coincidence between the radiologist's drawn blood vessel and the blood vessel segmented in this study. Greater accuracy in segmentation is achieved by increasing the value of Dice, which aims to maximise the overlap between the segmented vessels and the radiologist's delineation of the hepatic vessels. From equation (20) to equation (23), we have the following definitions of dice, accuracy, sensitivity, and specificity:

$$Dice = \frac{2TP}{2TP+FP+FN} \tag{20}$$

$$Accuracy = \frac{TP+TN}{TP+TN+FP+FN} \tag{21}$$

$$Sensitivity = \frac{TP}{TP+FN} \tag{22}$$

$$Specificity = \frac{TN}{TN+FP} \tag{23}$$

Some examples of these metrics are TP, which indicates the number of appropriately segmented blood vessel voxels; TN, which indicates the number of correctly voxels; besides FP, which indicates the number of wrongly segmented blood vessel voxels. FN is the total sum of voxels that have been mistakenly segmented as background, also known as false negatives.

IV.2 VALIDATION ANALYSIS OF PROPOSED SEGMENTATION ON FIRST DATASET.

Figure 7 demonstrations the comparative analysis of projected perfect with existing procedures such as TMPLiTS [17], ELTS-Net [18], DM-FF [20], AC-Net [21] and HTFCM [22], where the existing models uses different datasets and therefore, the study implements the basic models and results are averaged on first dataset.

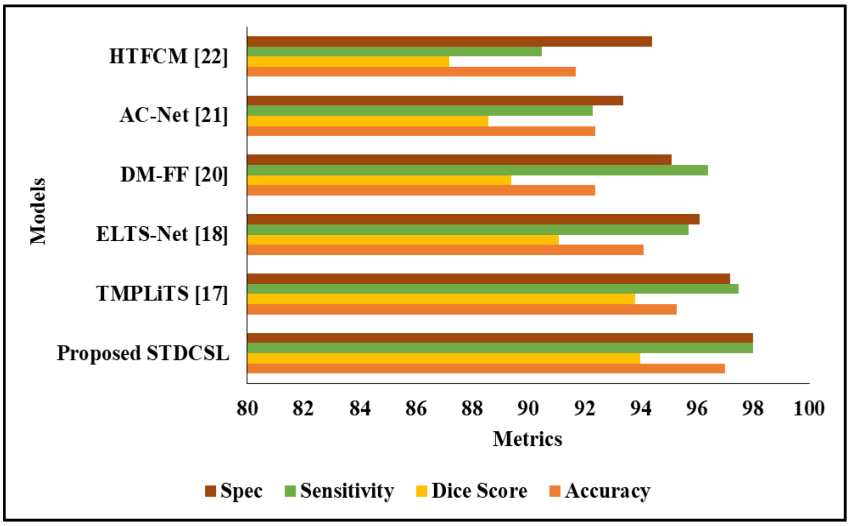

Figure 7: Graphical Comparison of projected with existing techniques on First dataset.
Source: Authors, (2026).

In the study of projected with existing techniques on First dataset of Proposed STDCSL scheme attained the accuracy as 97.0 and sensitivity of 94.0 also a dice score as 98.0 98.0 correspondingly. Then the TMPLiTS [17] scheme attained the accuracy as 95.3 and sensitivity of 93, also a dice score as 97.5 also a dice score as 97.2 correspondingly. Then the ELTS-Net [18] scheme attained the accuracy as 94.1 also a dice score as 91.1 and sensitivity of 95.7 also specificity as 96.1 correspondingly. Then the DM-FF [20] scheme attained the accuracy as 92.4 and sensitivity of 89.4 96.4 also specificity as 95.1 correspondingly. Then the AC-Net [21] scheme attained the accuracy as 92.4 and sensitivity of 88.6 also a dice score as 92.3 also specificity as 93.4 correspondingly. Then the HTFCM [22] scheme attained the accuracy as 91.7 and sensitivity of 87.2 also a dice score as 90.5 also specificity as 94.4 correspondingly.

IV.3 VALIDATION ANALYSIS OF PROPOSED SEGMENTATION ON SECOND DATASET

By using second dataset, the validation study of the projected is compared with existing procedures in terms of numerous metrics and it is shown in Figure 8.

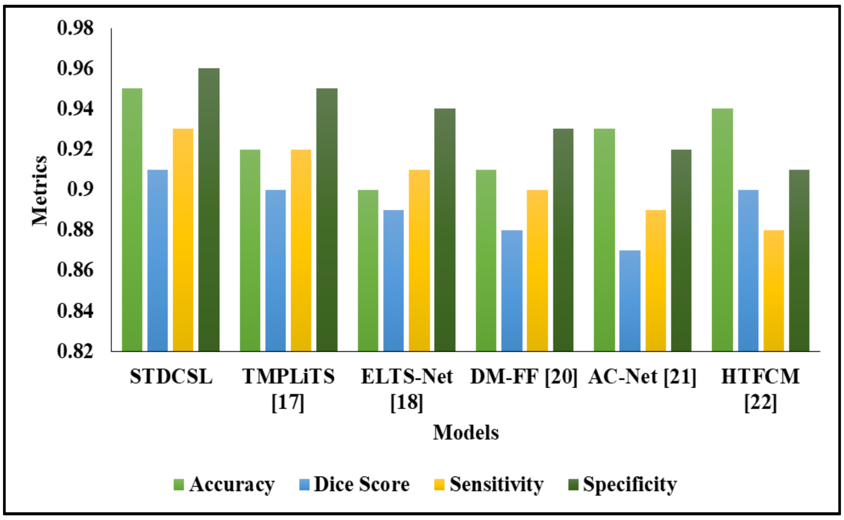

Figure 8: Visual Representation of different models.
Source: Authors, (2026).

In the experimental analysis of STDCSL scheme attained the accuracy as 0.95 also a dice score as 0.91 and sensitivity of 0.93 and sensitivity of 0.96 correspondingly. Then the TMPLiTS [17] scheme attained the accuracy as 0.92 also a dice score as 0.90 and sensitivity of 0.92 and sensitivity of 0.95 correspondingly. Then the ELTS-Net [18] scheme attained the accuracy as 0.90 also a dice score as 0.89 also a dice score as 0.91 and sensitivity of 0.94 correspondingly. Then the DM-FF [20] scheme attained the accuracy as 0.91 also a dice score as 0.88 also a dice score as 0.90 and sensitivity of 0.93 correspondingly. Then the AC-Net [21] scheme attained the accuracy as 0.93 also a dice score as 0.87 also a dice score as 0.89 and sensitivity of 0.92 correspondingly. Then the HTFCM [22] scheme attained the accuracy as 0.94 0.90 also a dice score as 0.88 and sensitivity of 0.91 correspondingly.

IV.4 VALIDATION ANALYSIS OF FINE-TUNER OPTIMIZATION ALGORITHM

To test the presentation of the projected fine-tuner classical, Figure 9 provides the graphical description with existing procedures.

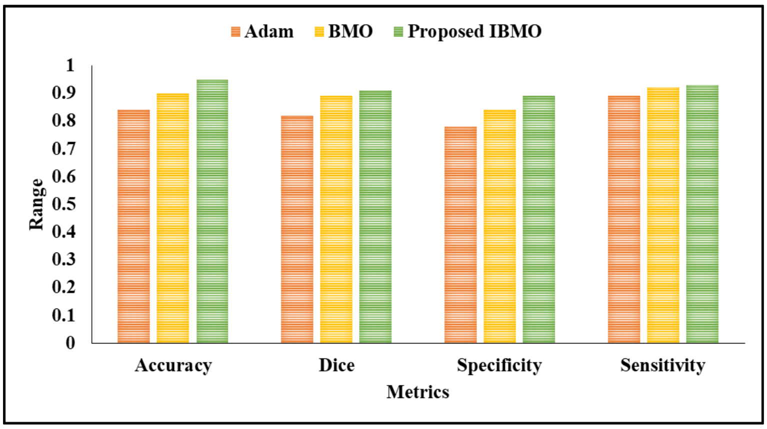

Figure 9: Graphical Description of the different models.
Source: Authors, (2026).

In the analysis of Adam scheme attained the accuracy as 0.84 and dice value of 0.82 also specificity as 0.78 and sensitivity of 0.89 correspondingly. Then the BMO scheme accomplished the accuracy as 0.90 also specificity as 0.89 also specificity as 0.84 and sensitivity of 0.92 correspondingly. Then the Projected IBMO scheme attained the accuracy as 0.95 also specificity as 0.91 also specificity as 0.89 and sensitivity of 0.93 correspondingly. Improved algorithms can potentially detect tumors at earlier stages, increasing the chances of successful treatment and better patient outcomes. More accurate imaging helps in creating personalized treatment plans that are tailored to the specific anatomy and condition of the patient.

V. CONCLUSION

Based on the STDC net, the study suggests the STDCSL model for semantic liver segmentation, which can adapt to the features of input photos. One benefit of this approach is that it can enhance segmentation minor impacted areas without producing a lot of unnecessary subtractions. Results from numerous trials and visualisations show that the STDCSL network is effective. A publicly available dataset of hepatic arteries has been used to demonstrate the efficacy of the strategy suggested in this study. Our suggested network model performs better than competing models in the mainstream. Segmenting the intricate hepatic blood veins from CT scans is a breeze with the suggested network model. More clinically relevant segmentation is the end consequence. Our present method has its drawbacks, such as being too dependent on diverse and high-quality training data, lacking confirmation of its generalizability on a larger scale, and lacking performance improvements.

To discourse these issues, our future research will focus on three main areas. Our primary objective is to explore the possibility of using synthetic tumours to train classifier models, as the expense of annotating images actual liver tumours is quite significant. This method is attractive for clinical use because it has the potential to significantly cut deployment costs while simultaneously improving efficiency. Owing to the enormous impact of analytic patient, the vital importance of understandable AI (XAI) representations in medical areas, especially in medical image processing, will be emphasised secondly. Thirdly, we intend to improve model presentation by combining conventional and neural approaches; specifically, we will investigate transformer-based models for automated liver tumour picture segmentation.

VI. AUTHOR’S CONTRIBUTION

Conceptualization: Selvakumar Subramanian, Dr. Sivakumar S, Dr. K. R. Ananthapadmanaban.
Methodology: Selvakumar Subramanian, Dr. Sivakumar S, Dr. K. R. Ananthapadmanaban.
Investigation: Selvakumar Subramanian, Dr. Sivakumar S, Dr. K. R. Ananthapadmanaban.
Discussion of results: Selvakumar Subramanian, Dr. Sivakumar S, Dr. K. R. Ananthapadmanaban.
Writing – Original Draft: Selvakumar Subramanian, Dr. Sivakumar S, Dr. K. R. Ananthapadmanaban.
Writing – Review and Editing: Selvakumar Subramanian, Dr. Sivakumar S, Dr. K. R. Ananthapadmanaban.
Resources: Selvakumar Subramanian, Dr. Sivakumar S, Dr. K. R. Ananthapadmanaban.
Supervision: Selvakumar Subramanian, Dr. Sivakumar S, Dr. K. R. Ananthapadmanaban.
Approval of the final text: Selvakumar Subramanian, Dr. Sivakumar S, Dr. K. R. Ananthapadmanaban.

VII. REFERENCES

[1] Saha Roy, S., Roy, S., Mukherjee, P., & Halder Roy, A. (2023). An automated liver tumour segmentation and classification model by deep learning based approaches. Computer Methods in Biomechanics and Biomedical Engineering: Imaging & Visualization, 11(3), 638-650.

[2] Hossain, M. S. A., Gul, S., Chowdhury, M. E., Khan, M. S., Sumon, M. S. I., Bhuiyan, E. H., ... & Alqahtani, A. (2023). Deep Learning Framework for Liver Segmentation from T 1-Weighted MRI Images. Sensors, 23(21), 8890.

[3] Gunapriya, B., Rajesh, T., Thirumalraj, A., & Manjunatha, B. (2023). LW-CNN-based extraction with optimized encoder-decoder model for detection of diabetic retinopathy. FRONTIER SCIENTIFIC PUBLISHING PTE. LTD, 1095.

[4] Wang, J., Peng, Y., Jing, S., Han, L., Li, T., & Luo, J. (2023). A deep-learning approach for segmentation of liver tumors in magnetic resonance imaging using UNet++. BMC cancer, 23(1), 1060.

[5] Bilic, P., Christ, P., Li, H. B., Vorontsov, E., Ben-Cohen, A., Kaissis, G., ... & Menze, B. (2023). The liver tumor segmentation benchmark (lits). Medical Image Analysis, 84, 102680.

[6] Kushnure, D. T., Tyagi, S., & Talbar, S. N. (2023). LiM-Net: Lightweight multi-level multiscale network with deep residual learning for automatic liver segmentation in CT images. Biomedical Signal Processing and Control, 80, 104305.

[7] Thirumalraj, A., Anusuya, V. S., & Manjunatha, B. (2024). Detection of Ephemeral Sand River Flow Using Hybrid Sandpiper Optimization-Based CNN Model. In Innovations in Machine Learning and IoT for Water Management (pp. 195-214). IGI Global.

[8] Liu, H., Fu, Y., Zhang, S., Liu, J., Wang, Y., Wang, G., & Fang, J. (2023). GCHA-Net: Global context and hybrid attention network for automatic liver segmentation. Computers in Biology and Medicine, 152, 106352.

[9] Konkel, B., Macdonald, J., Lafata, K., Zaki, I. H., Bozdogan, E., Chaudhry, M., ... & Bashir, M. R. (2023). Systematic Analysis of Common Factors Impacting Deep Learning Model Generalizability in Liver Segmentation. Radiology: Artificial Intelligence, 5(3), e220080.

[10] Oh, N., Kim, J. H., Rhu, J., Jeong, W. K., Choi, G. S., Kim, J. M., & Joh, J. W. (2023). Automated 3D liver segmentation from hepatobiliary phase MRI for enhanced preoperative planning. Scientific Reports, 13(1), 17605.

[11] Lakshmipriya, B., Pottakkat, B., & Ramkumar, G. (2023). Deep learning techniques in liver tumour diagnosis using CT and MR imaging-A systematic review. Artificial Intelligence in Medicine, 141, 102557.

[12] Xie, T., Li, Y., Lin, Z., Liu, X., Zhang, X., Zhang, Y., ... & Wang, X. (2023). Deep learning for fully automated segmentation and volumetry of couinaud liver segments and future liver remnants shown with CT before major hepatectomy: a validation study of a predictive model. Quantitative Imaging in Medicine and Surgery, 13(5), 3088.

[13] Mourya, G. K., Gogoi, M., Talbar, S. N., Dutande, P. V., & Baid, U. (2023). Cascaded dilated deep residual network for volumetric liver segmentation from CT image. In Research Anthology on Improving Medical Imaging Techniques for Analysis and Intervention (pp. 1153-1165). IGI Global.

[14] Wesdorp, N. J., Zeeuw, J. M., Postma, S. C., Roor, J., van Waesberghe, J. H. T., van den Bergh, J. E., ... & Kazemier, G. (2023). Deep learning models for automatic tumor segmentation and total tumor volume assessment in patients with colorectal liver metastases. European radiology experimental, 7(1), 75.

[15] Ifty, M. A. H., & Shajid, M. S. S. (2023, February). Implementation of liver segmentation from computed tomography (ct) images using deep learning. In 2023 International Conference on Electrical, Computer and Communication Engineering (ECCE) (pp. 1-6). IEEE.

[16] Dickson, J., Linsely, A., & Nineta, R. A. (2023). An integrated 3D-sparse deep belief network with enriched seagull optimization algorithm for liver segmentation. Multimedia Systems, 29(3), 1315-1334.

[17] Hu, C., Xia, T., Cui, Y., Zou, Q., Wang, Y., Xiao, W., ... & Li, X. (2024). Trustworthy multi-phase liver tumor segmentation via evidence-based uncertainty. Engineering Applications of Artificial Intelligence, 133, 108289.

[18] Guo, X., Wang, Z., Wu, P., Li, Y., Alsaadi, F. E., & Zeng, N. (2024). ELTS-Net: An enhanced liver tumor segmentation network with augmented receptive field and global contextual information. Computers in Biology and Medicine, 169, 107879.

[19] Wang, K. N., Li, S. X., Bu, Z., Zhao, F. X., Zhou, G. Q., Zhou, S. J., & Chen, Y. (2024). Sbcnet: Scale and boundary context attention dual-branch network for liver tumor segmentation. IEEE Journal of Biomedical and Health Informatics.

[20] Xu, C., Wu, X., Wang, B., Chen, J., Gao, Z., Liu, X., & Zhang, H. (2024). Accurate segmentation of liver tumor from multi-modality non-contrast images using a dual-stream multi-level fusion framework. Computerized Medical Imaging and Graphics, 102414.

[21] Shao, J., Luan, S., Ding, Y., Xue, X., Zhu, B., & Wei, W. (2024). Attention Connect Network for Liver Tumor Segmentation from CT and MRI Images. Technology in Cancer Research & Treatment, 23, 15330338231219366.

[22] Bhimavarapu, U. (2024). Automatic liver tumor detection and classification using the hyper tangent fuzzy C-Means and improved fuzzy SVM. Multimedia Tools and Applications, 83(15), 46201-46220.

[23] Prabaharan, G., Dhinakaran, D., Raghavan, P., Gopalakrishnan, S., & Elumalai, G. (2024). AI-Enhanced Comprehensive Liver Tumor Prediction using Convolutional Autoencoder and Genomic Signatures. International Journal of Advanced Computer Science & Applications, 15(2).

[24] P. Bilic et al., "The liver tumor segmentation benchmark (lits)," vol. 84, p. 102680, 2023.

[25] Sabir, M. W., Khan, Z., Saad, N. M., Khan, D. M., Al-Khasawneh, M. A., Perveen, K., ... & Azhar Ali, S. S. (2022). Segmentation of liver tumor in CT scan using ResU-Net. Applied Sciences, 12(17), 8650.

[26] Khalifa, N.E.; Loey, M.; Mirjalili, S. A comprehensive survey of recent trends in deep learning for digital images augmentation. Artif. Intell. Rev. 2021, 55, 2351–2377.

[27] Zhou, X.Y.; Yang, G.Z. Normalization in training U-Net for 2-D biomedical semantic segmentation. IEEE Robot. Autom. Lett. 2019, 4, 1792–1799.

[28] Yu, C.; Wang, J.; Peng, C.; Gao, C.; Yu, G.; Sang, N. Bisenet: Bilateral segmentation network for real-time semantic segmentation. In Proceedings of the European Conference on Computer Vision (ECCV), Munich, Germany, 8–14 September 2018; pp. 325–341.

[29] Xu, J.; Xiong, Z.; Bhattacharyya, S.P. Pidnet: A real-time semantic segmentation network inspired from pid controller. arXiv 2022, arXiv:2206.02066.

[30] Sulaiman, M. H., Mustaffa, Z., Saari, M. M., & Daniyal, H. (2020). Barnacles mating optimizer: a new bio-inspired algorithm for solving engineering optimization problems. Engineering Applications of Artificial Intelligence, 87, 103330.